International Journal of Nanomedicine

Dovepress
open access to scientific and medical research

Open Access Full Text Article

ORIGINAL RESEARCH

Optimizing particle size for targeting diseased microvasculature: from experiments to artificial neural networks

This article was published in the following Dove Press journal:
International Journal of Nanomedicine
18 July 2011
Number of times this article has been viewed

Daniela P Boso[1]
Sei-Young Lee[2]
Mauro Ferrari[3]
Bernhard A Schrefler[1]
Paolo Decuzzi[3]

[1]Department of Structural and Transportation Engineering, University of Padova, Padova, Italy; [2]Global Production Technology Center, Samsung Electronics Co Ltd, Republic of Korea; [3]The Methodist Hospital Research Institute, Department of Nanomedicine and Biomedical Engineering, Houston, TX, USA

Background: Nanoparticles with different sizes, shapes, and surface properties are being developed for the early diagnosis, imaging, and treatment of a range of diseases. Identifying the optimal configuration that maximizes nanoparticle accumulation at the diseased site is of vital importance. In this work, using a parallel plate flow chamber apparatus, it is demonstrated that an optimal particle diameter (d_{opt}) exists for which the number (n_s) of nanoparticles adhering to the vessel walls is maximized. Such a diameter depends on the wall shear rate (S). Artificial neural networks are proposed as a tool to predict n_s as a function of S and particle diameter (d), from which to eventually derive d_{opt}. Artificial neural networks are trained using data from flow chamber experiments. Two networks are used, ie, ANN231 and ANN2321, exhibiting an accurate prediction for n_s and its complex functional dependence on d and S. This demonstrates that artificial neural networks can be used effectively to minimize the number of experiments needed without compromising the accuracy of the study. A similar procedure could potentially be used equally effectively for in vivo analysis.

Keywords: nanoparticle, optimal configuration, vascular adhesion, laminar flow, wall shear rate, artificial neural networks

Introduction

The use of nanoparticles in the early diagnosis, treatment, and imaging of a number of disorders, such as cancer and cardiovascular disease, is emerging as a powerful tool.[1] Sufficiently small nanoparticles can be administered at the systemic level, transported by blood flow, and reach potentially any site within the macrovascular and microvascular circulation carrying imaging and therapeutic agents. A large variety of nanoparticles have been developed, and exhibit differences in size, shape, surface physicochemical properties, material composition, and deformability.

In cancer treatment and imaging, the maximum nanoparticle diameter has been traditionally limited to 200–300 nm in order to take full advantage of the well known enhanced permeation and retention effects.[2] Given that tumor vasculature has been shown to be discontinuous, with "fenestrations" a few hundred nanometers in size, sufficiently small nanoparticles would more likely extravasate by crossing the fenestrations passively and accumulating in the tumor interstitium.[3–5] Within this size range, many different nanoparticle types have been proposed including liposomes and polymeric particles,[6] dendrimers with a characteristic size of 4–10 nm,[7] super paramagnetic iron oxide particles for cancer imaging and magnetic hyperthermia,[8] gold nanoshells for photothermal therapy,[9] and nanoporous silica beads for drug delivery and imaging.[10]

Correspondence: Paolo Decuzzi
The Methodist Hospital Research Institute, Department of Nanomedicine and Biomedical Engineering,
6670 Bertner Ave, Houston,
TX 77030, USA
Tel +1 713 441 7316
Fax +1 713 441 7438
Email pdecuzzi@tmhs.org

submit your manuscript | www.dovepress.com
Dovepress
http://dx.doi.org/10.2147/IJN.S20283

However, enhanced permeation and retention-based delivery strategies are recognized to have important limitations, ie, the fenestration size varies with the type, location, and stage of the disease, and indeed with the patient.[3] Most importantly, vascular fenestrations are cancer-specific and are not found in other diseases directly involving the vascular apparatus, eg, atheroma. Here, we consider a more general nanoparticle delivery strategy based on targeting the diseased vasculature without relying on fenestrations and the enhanced permeation and retention effect. In this case, nanoparticles were designed to recognize and adhere efficiently to the walls of the diseased blood vessels and to resist dislodging hydrodynamic forces.

Mathematical models have been proposed to predict the probability of vascular adhesion as a function of nanoparticle size, shape, and surface properties, and biophysical conditions at the site of adhesion.[11,12] By contrast, in this work artificial neural networks in conjunction with flow chamber experiments are proposed as a tool to predict and optimize vascular adhesion of nanoparticles.

Methods and materials

Spherical particles and flow chamber apparatus

Polystyrene fluorescent particles (Fluoresbrite®, Polysciences, Warrington, PA) of different sizes were purchased, namely 0.75, 1.0, 2.0, 4.5, and 6.0 µm (nominal diameter). Particle number and diameter were measured using a Multisizer 4 Coulter Counter and a size analyzer (Beckman Coulter, Fullerton, CA) with a 100 µm aperture. Particles were suspended in a balanced electrolyte solution (ISOTON II Diluent, Beckman Coulter) and counted. The surface zeta potential was measured using a ZetaPALS (Brookhaven, NY). The actual particle diameter and surface zeta potential are listed in Table 1.

The adhesion experiments were conducted in a parallel plate flow chamber (Glycotech, Rockville, MD) consisting of a Plexiglass flow deck, with inlet and outlet holes, a 35 mm borosilicate cover slip, and a silicon gasket, installed between the flow deck and the cover slip. The parallel plate flow chamber was connected to a syringe pump (Harvard Apparatus, Holliston, MA) through plastic tubing to control the flow rate precisely. The chamber channel was 5 mm wide (w), 20 mm long (l), and 254 µm high (h). After connecting the chamber to the pump, the apparatus was placed on the stage of an inverted fluorescent microscope (Nikon TE-2000). A schematic of the apparatus is presented in Figure 1.

For each experiment, 10^6 fluorescent polystyrene particles in 1 mL of solution were injected at different shear rates (S = 50, 75, and 90 sec^{-1}), controlled through the syringe pump flow rate Q following the relationship:

$$S = \frac{6Q}{h^2 w} \tag{1}$$

Experiments were performed at room temperature (25°C). Images of the fluorescent particles adhering to the substrate within the chamber were captured at regions of interest using a 20× dry objective and were saved to a computer for storage. Multiple regions of interest were chosen in the middle of the channel to limit flow disturbance due to the side walls and inlet/outlet effects. The still images were saved to a computer for storage using a Nikon DQC-FS digital camera (Tokyo, Japan), and exported as TIF files into ImageJ, a freeware software from the National Institutes of Health (http://rsb.info.nih.gov/ij/), for postprocessing.

The 35 mm borosilicate dishes were coated with collagen type I solution from rat tails (Sigma-Aldrich Corporation, St Louis, MO). The collagen solution with a concentration of 4 mg/mL was diluted in double-distilled water to obtain a surface coverage of about 10 µg/cm². After coating, the cover slips were kept at 4°C overnight before running the experiments.

Artificial neural networks

The basics of artificial neural networks are briefly covered below. A more comprehensive description is given elsewhere.[13,14] The artificial neural network is a mathematical/computational tool, inspired by the structural and functional properties of the biological neural network, and consists of a collection of processing units (nodes or neurons) organized into layers and mutually interconnected through connecting links (synapses, see Figure 2A and 2B). In artificial neural networks, there are three distinct types of layers: the input layer, comprising all the input nodes; the hidden layer(s) collecting the processing nodes; and the output layer, comprising all the output nodes. In this work, fully connected networks are used where all the nodes in each

Table 1 Size and zeta potential of polystyrene carboxylate fluorescent microspheres

$D_{nominal}$ (µm)	0.75	1.00	2.00	4.50	6.00
$D_{measured}$ (µm)	0.72	0.97	1.83	4.90	6.60
Zeta potential (mV)	−73.1 ± 2.5	−87.3 ± 3.1	−70.6 ± 4.4	−82.2 ± 7.0	−52.4 ± 0.4

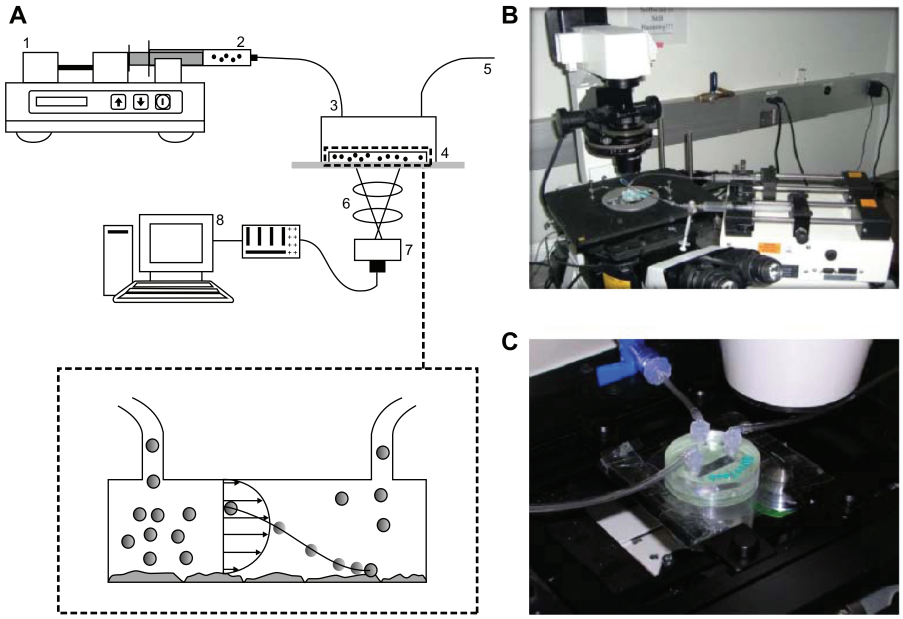

Figure 1 (**A**) Parallel plate flow chamber apparatus, used for in vitro adhesion experiments, consisting of: 1, a syringe pump; 2, a syringe with particles suspended in solution; 3, inlet tubing; 4, parallel plate flow chamber; 5, outlet tubing; 6, microscope; 7, digital camera; and 8, computer. (**B**) Images depicting an epifluorescent microscope with setup of the system, and (**C**) the parallel plate flow chamber with tubing network installed over the stage of the microscope.

layer receive connections from all the nodes in the preceding layer. Information enters the network through the input nodes, is then passed to the sets of hidden layers, and eventually reaches the output nodes. A synapsis connecting node *i* to *j* is characterized by a weighting function (w_{ij}); and each layer (r) is characterized by a bias function (b_r), which is equally applied to all nodes within the same layer. The information reaching a node *j* is weighted, combined, and processed through a transfer function (g_r). The transfer function serves to normalize the information leaving node *j*. In mathematical terms, the artificial neural networks are defined in equation (2) where *i* and *o* are, respectively, the input and output vectors. Equation (2) is written for the *j*-th output from a network consisting of three layers (input, hidden layer, and output, Figure 2A). The weights $w_{ij}^{(l)}$ are identified by the layer number (superscript *l*) and node numbers (subscripts *i* and *j*); the bias functions $b_j^{(l)}$ are identified by the layer number (Figure 2B). Summation over repeated indexes is used, except when the index is enclosed by parentheses (layer number). This kind of network has been described elsewhere.[15–18]

$$o_j = \sum_s w_{js}^{(3)} g_s\left(\sum_r w_{sr}^{(2)} g_r\left(\sum_i w_{ri}^{(1)} i_i + b_r^{(1)}\right) + b_s^{(2)}\right) + b_j^{(3)} \tag{2}$$

During the training process, the weights (w_{ij}) are modified by an iterative procedure to align the output signal with the

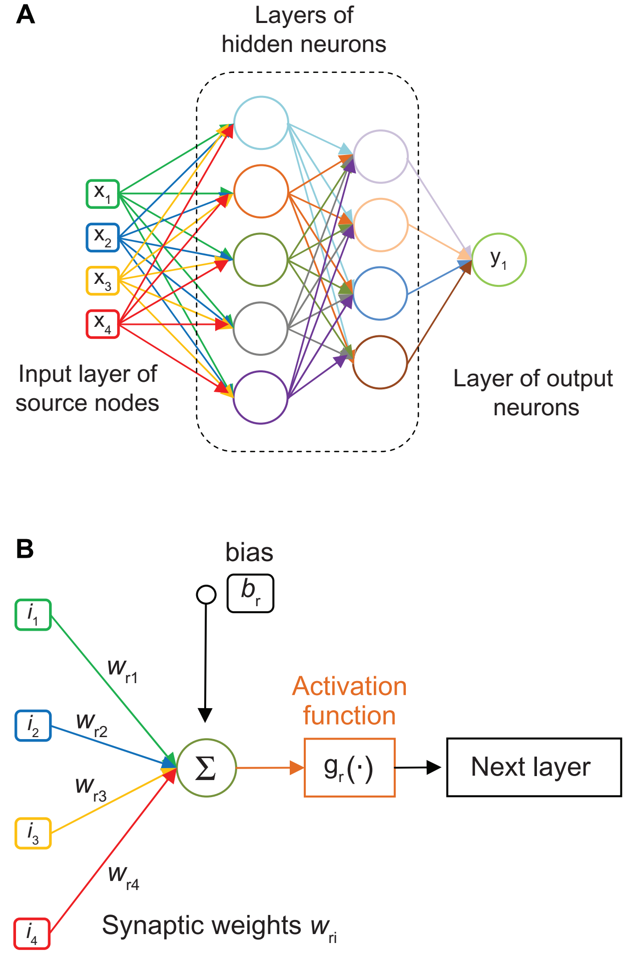

Figure 2 (**A**) Fully connected neural network with two hidden layers. (**B**) Typical scheme of a neuron and its activity: $g_r(\sum_i w_{ri} i_i + b_r)$.

experimental data (test data set). In this phase, a proper set of input–output data is specified and used partly to define weights and biases (learning set), and partly (test set) to check the error of the network response. Once the artificial neural network is trained, it is used in recall mode to predict the behavior of the system.

Although different transfer functions (g) can be used (ie, sigmoid, gaussian, hyperbolic tangent, and hyperbolic secant functions), the sigmoid transfer function $1/(1+e^{-x})$ is used here for all layers. The sigmoid function has been shown to provide good learning characteristics and excellent accuracy.[19] Also, concerning the topology of the network, one to four hidden layers are usually sufficient in the vast majority of cases. Complex functional relationships can be more accurately modeled with a higher number of layers, but at the expense of computational and training time.

Results

Flow chamber experiment and optimal particle size

After injection into the parallel plate flow chamber system, the number (n_s) of particles adhering per unit area to the collagen substrate was measured using fluorescence microscopy under different hydrodynamic conditions (wall shear rate S) and particle diameter (d). These results are shown in Figure 3. For a fixed diameter (d), the number (n_s) of adhering particles decreases steadily as S grows; whereas for a fixed S ranging between 50 and 90 per second the functional dependence of n_s on d is more complicated, exhibiting a maximum and correspondingly optimal diameter (d_{opt}).

Particle adhesion is regulated by the interplay between hydrodynamic forces and adhesive interactions arising at the particle/substrate interface.[14] The hydrodynamic forces exerted over a spherical particle attached to a rigid wall in a linear laminar flow are given by:[11]

$$F = \frac{3}{2}\pi d^2 \mu S F^s \quad \text{and} \quad T = \frac{\pi}{2} d^3 \mu S T^s$$
$$(F^s \approx 1.668 \quad \text{and} \quad T^s \approx 0.944) \qquad (3)$$

whereas the adhesive interactions are related in a complex way to the particle diameter (d).[11] As the shear rate (S) increases, for a given d, the hydrodynamic forces (F) and (T) increase too and would tend to dislodge the particle away from the substrate, justifying the $n_s(S)$ relationship. Such a biphasic behavior was predicted for the first time by Decuzzi and Ferrari.[12] Here, for the first time, it is experimentally demonstrated that an optimal size (d_{opt}) exists, for which the number of adhering particles (n_s) is maximized.

In the case at hand, the nonsymbolic model is constructed as follows. First, a suitable neural network is trained with a known input–output data set, which is obtained from the parallel plate flow chamber experiments described above. Then the network generalization capability enables prediction of n_s for an arbitrary sequence of the particle size (d) and wall shear rate (S).

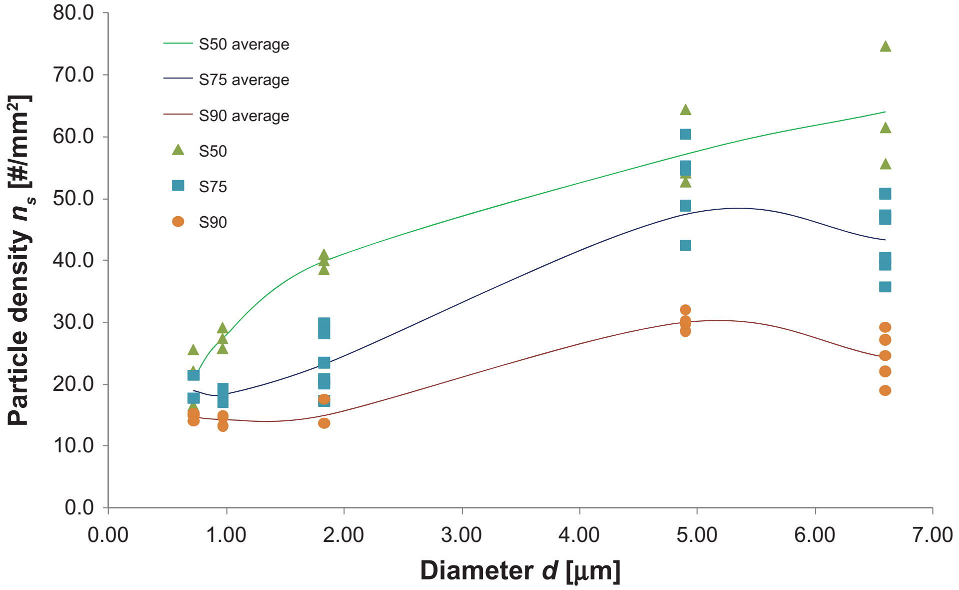

Figure 3 Number of particles (n_s) adhering per unit area in a parallel plate flow chamber, under different flow conditions (shear rate to the wall [S]), as a function of particle diameter d. Single marks represent the experimental data, as from Table S1.

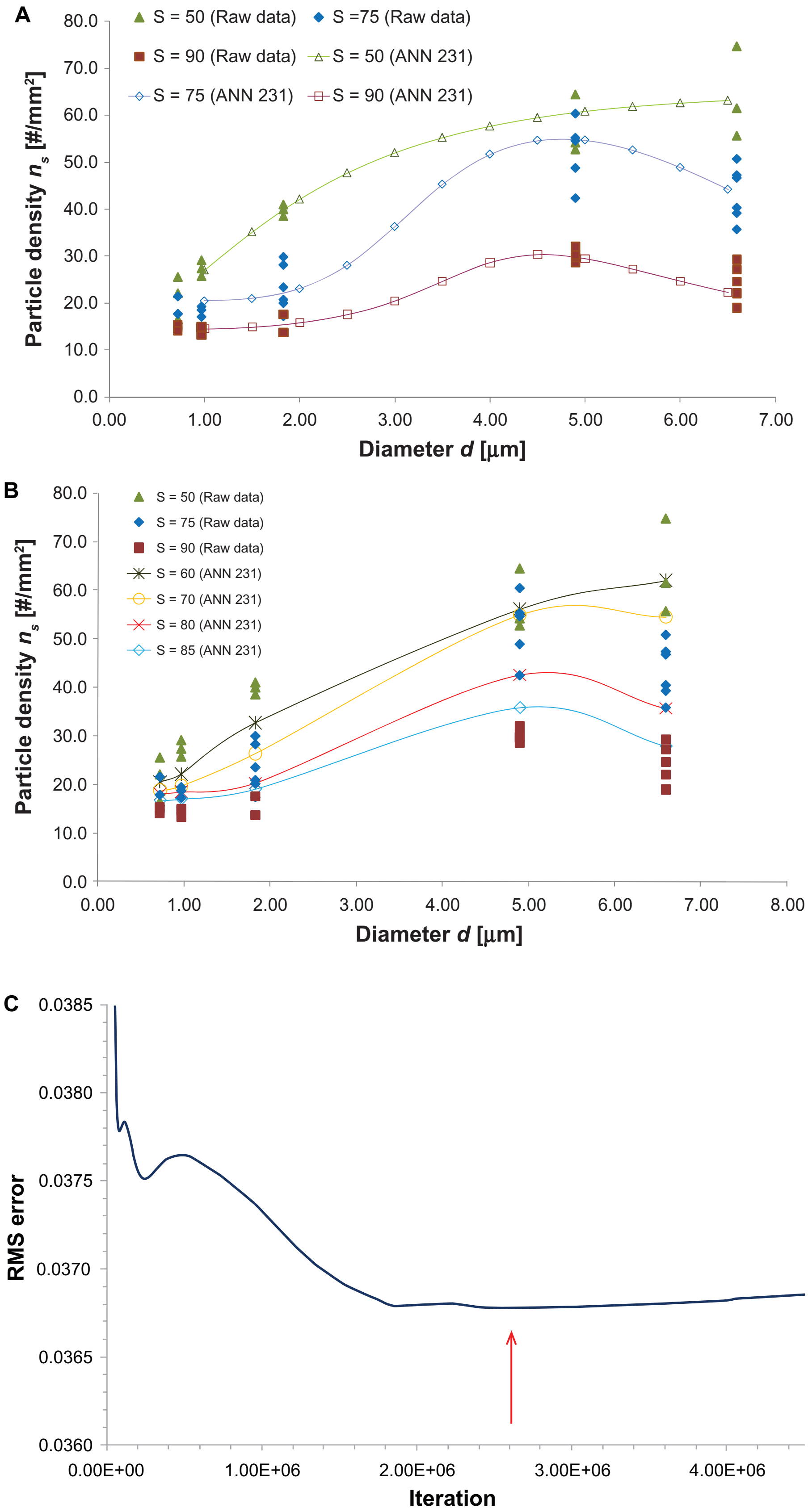

Figure 4 (**A**) The $n_s(d)$ relationship as predicted from ANN231 for particle diameters not tested in the experiments. (**B**) The $n_s(d)$ relationship as predicted from ANN231 for shear rates (*S*) not tested in the experiments. (**C**) Root mean squared error of the test set of data for the ANN231.

Note: The red arrow depicts the minimum (2.6×10^6 iterations).

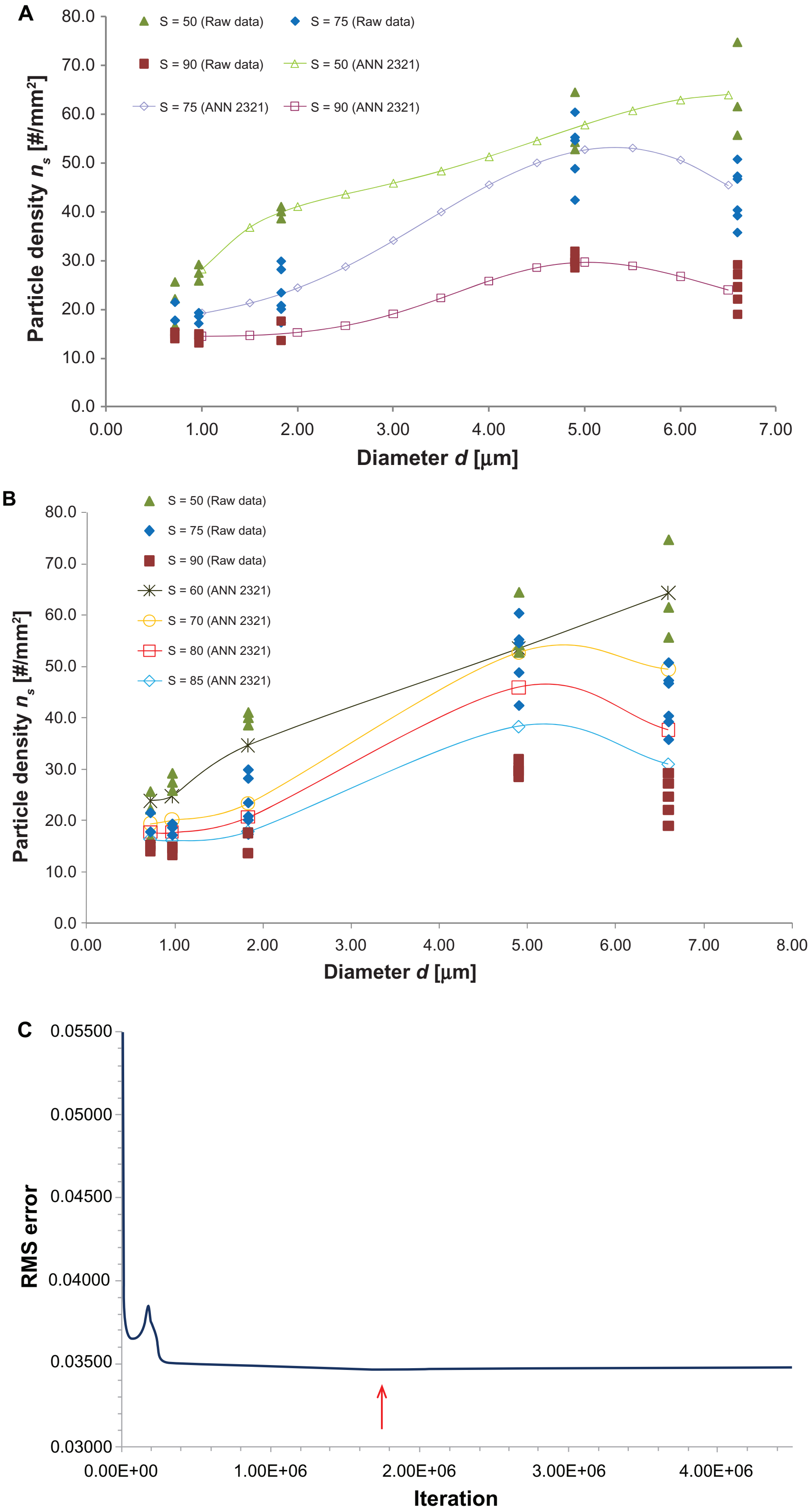

Figure 5 (**A**) The $n_s(d)$ relationship as predicted from ANN2321 for particle diameter not tested in the experiments. (**B**) The $n_s(d)$ relationship as predicted from ANN2321 for shear rates *S* not tested in the experiments. (**C**) Root mean squared error of the test set of data for the ANN2321.
Note: The red arrow depicts the minimum (1.75 × 10^6 iterations).

Artificial neural networks for predicting optimal particle size

Any arbitrary complex function can be approximated by an artificial neural network,[20] but in a nonconstructive manner. This implies that the number of internal degrees of freedom (ie, number of hidden layers, total number of nodes, node repartition between hidden layers) for the best approximation of an artificial neural network needs to be defined by the user. In this work, artificial neural networks with one and two hidden layers were considered, namely ANN231 (one hidden layer with three nodes) and ANN2321 (two hidden layers with three and two nodes). The experimental data used for training the networks are listed in supplementary Table S1. The values for the mean (μ) and standard deviation (σ) for the experimentally measured number of particles adhering per unit area are listed in supplementary Table S2, as a function of the particle diameter (*d*) and wall shear rate (*S*).

Figure 4 presents the variation of n_s with *d* and *S* as predicted from the network ANN231. In Figure 4A, n_s is plotted for new values of *d* (1.0, 1.5, 2.0, 2.5, 3.0, 3.5, 4.0, 4.5, 5.0, 5.5, 6.0, and 6.5 μm), not considered in the experiments, and for the shear rates $S = 50$, 75, and 90 per second which are the same as those tested experimentally. In Figure 4B, n_s is plotted for new values of *S,* not considered in the experiments, namely $S = 60$, 70, 80, and 85 per second and for particle diameters tested in the experiments. The network can capture the complexity of the experimental results, with optimal particle diameter (d_{opt}) reducing as *S* increases. Figure 4C presents the variation of the root mean squared error with the number of iterations. A minimum is observed for $2.6 \times 10^{+6}$ iterations. The results in Figure 5 are, respectively, the predictions (Figures 5A and 5B) and root mean squared error (Figure 5C) obtained using the network ANN2321, as described above for the previous network.

Table 2 Root mean squared error for learning and test sets of the two ANNs used

ANN	RMSE learning set	RMSE test set
231	0.04620	0.03678
2321	0.04623	0.03460

Abbreviations: ANN, artificial neural networks; RMSE, root mean squared error.

For different *d*, the ANN2321 provides predictions slightly closer to the experimental data than ANN231 (Figures 5A and 4A, respectively). In both cases, the accuracy of the predictions for the intermediate values of *S* (75 per second) is most critical. For different *S*, both networks give similarly accurate results (Figures 4B and 5B, respectively). The characteristic errors of the training processes are shown in Table 2 (root mean squared error for learning and test sets). It should be noted that, for each network, the training process should be stopped when the root mean squared error of the test set reaches a minimum (Figures 4C and 5C), with a still decreasing learning

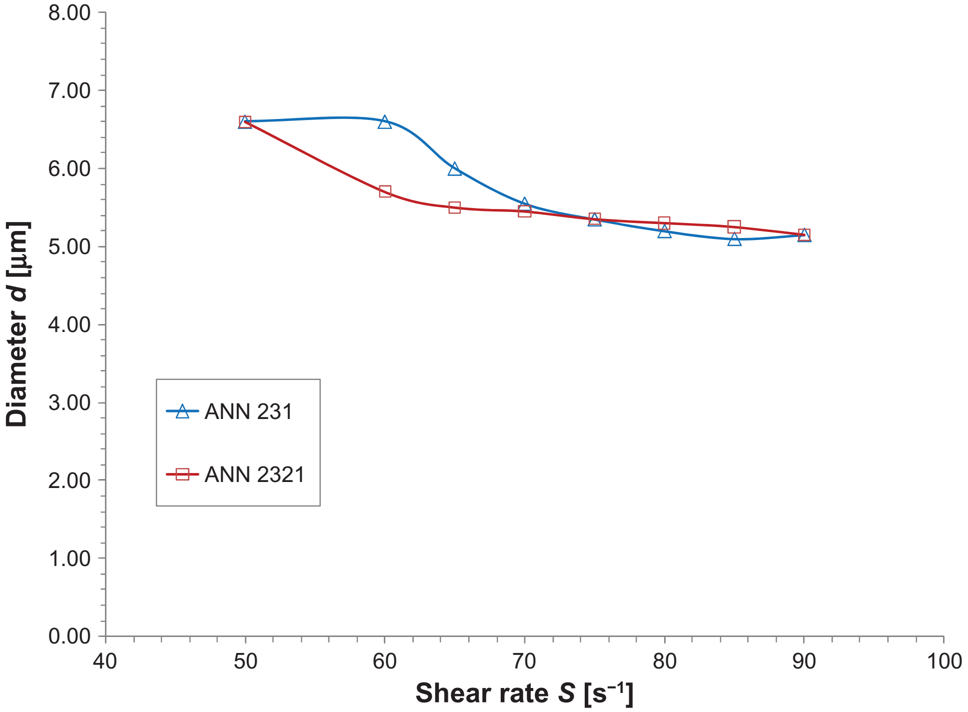

Figure 6 The optimal diameter d_{opt} as a function of *S* for the ANN231 and ANN2321.

root mean squared error (Figure S1 and Figure S2). However, given that the behavior of the test error for ANN2321 is substantially flat, we have used in this instance an "over-trained" version of it (ie, a very high number of iterations where neither the learning error nor the test error are changing).

Finally, the two proposed networks were used to predict the optimal particle size (d_{opt}) as a function of the shear rate (S). In both cases, d_{opt} reduced with S (Figure 6) in agreement with the experiments, but the ANN2321 has smoother behavior which captures the physics of the problem more appropriately.

Conclusion

Artificial neural networks were proposed to predict the number of particles adhering to the vasculature as a function of particle diameter (d) and wall shear rate (S). Two neural networks were considered with different internal structures (ANN231 and ANN2321), and their predictions were compared with the experimental data obtained by analyzing the adhesion performance of spherical nanoparticles injected into a parallel plate flow chamber system.

The proposed artificial neural networks captured the complexity of the physical problem, exhibiting biphasic behavior for the n_s (d) relationship, and demonstrating the existence of an optimal particle diameter (d_{opt}) for which the number of adhering particles is maximized. The ANN2321 offered slightly smaller characteristic errors than ANN231, and predicted more accurately the variation of d_{opt} with S. This work suggests that the number of long parallel plate flow chamber experiments can be reduced by using artificial neural networks, without compromising the accuracy of the study. This same procedure could be used for in vivo applications leading to a significant reduction in the number of animal experiments.

Disclosure

The authors report no conflicts of interest in this work.

References

1. Peer D, Karp JM, Hong S, Farokhzad OC, Margalit R, Langer R. Nanocarriers as an emerging platform for cancer therapy. *Nat Nanotechnol*. 2007;2:751–760.
2. Matsumura Y, Oda T, Maeda H. General mechanism of intratumor accumulation of macromolecules: advantage of macromolecular therapeutics. *Gan To Kagaku Ryoho*. 1987;14:821–829. Japanese.
3. Jain RK. Barriers to drug-delivery in solid tumors. *Sci Am.* 1994;271:58–65.
4. Yuan F, Leunig M, Huang SK, Berk DA, Papahadjopoulos D, Jain RK. Microvascular permeability and interstitial penetration of sterically stabilized (stealth) liposomes in a human tumor xenograft. *Cancer Res*. 1994;54:3352–3356.
5. Yuan F, Dellian M, Fukumura D, et al. Vascular permeability in a human tumor xenograft: molecular size dependence and cutoff size. *Cancer Res*. 1995;55:3752–3756.
6. Torchilin VP. Multifunctional nanocarriers. *Adv Drug Deliv Rev*. 2006;58:1532–1555.
7. Kukowska-Latallo JF, Candido KA, Cao Z, et al. Nanoparticle targeting of anticancer drug improves therapeutic response in animal model of human epithelial cancer. *Cancer Res*. 2005;65:5317–5324.
8. Thorek DL, Chen AK, Czupryna J, Tsourkas A. Super paramagnetic iron oxide nanoparticle probes for molecular imaging. *Ann Biomed Eng*. 2006;34:23–38.
9. Hirsch LR, Gobin AM, Lowery AR, et al. Metal nanoshells. *Ann Biomed Eng*. 2006;34:15–22.
10. Park JH, Gu L, von Maltzahn G, Ruoslahti E, Bhatia SN, Sailor MJ. Biodegradable luminescent porous silicon nanoparticles for in vivo applications. *Nat Mater*. 2009;8:331–336.
11. Goldman AJ, Cox RG, Brenner H. Slow viscous motion of a sphere parallel to a plane wall-I motion through a quiescent fluid. *Chem Eng Sci*. 1967;22:637–651.
12. Decuzzi P, Ferrari M. The adhesive strength of non-spherical particles mediated by specific interaction. *Biomaterials*. 2006;27:5307–5314.
13. Hertz J, Krogh A, Palmer GR. *Introduction to the Theory of Neural Computation*. Boston, MA: Addison-Wesley Longman Publishing; 1991.
14. Hu YH, Hwang JN, editors. *Handbook of Neural Network Signal Processing*. Boca Raton, FL: CRC Press; 2002.
15. Lefik M, Schrefler BA. Artificial neural network for parameter identifications for an elasto-plastic model of super conducting cable under cyclic loading. *Computers and Structures*. 2002;80;1699–1713.
16. Lefik M, Schrefler BA. Artificial neural network as an incremental non-linear constitutive model for a finite element code. *Comput Methods Appl Mech Eng*. 2003;192:3265–3283.
17. Lefik M, Boso DP, Schrefler BA. Artificial neural networks in numerical modelling of composites. *Comput Methods Appl Mech Eng*. 2009;198:1785–1804.
18. Lefik M, Boso DP. Numerical phenomenology: virtual testing of the hierarchical structure of a bundle of strands. *Computer Modelling in Engineering and Sciences*. 2010;55:319–337.
19. Haykin S. *Neural Networks*. 2nd ed. Upper Saddle River, NJ: Prentice Hall International; 1999.
20. Chen T, Chen H. Universal approximation to non-linear operators by neural networks with arbitrary activation functions and its application to dynamical systems. *IEEE Trans Neural Netw*. 1995;6:911–917.

Supplementary material

Table S1 Experimental data for the number of particles n_s adhering per unit area in a parallel plate flow chamber

S [sec^{-1}]	d [µm]	n_s[#/mm^2]
50	0.720	25.60
50	0.720	16.56
50	0.720	22.13
50	0.968	25.79
50	0.968	29.16
50	0.968	27.40
50	1.829	40.01
50	1.829	38.57
50	1.829	41.04
50	4.899	64.49
50	4.899	52.76
50	4.899	54.23
50	6.596	61.55
50	6.596	55.70
50	6.596	74.75
75	0.720	17.78
75	0.720	21.50
75	0.720	17.78
75	0.968	17.15
75	0.968	19.35
75	0.968	18.61
75	1.829	17.30
75	1.829	20.81
75	1.829	20.08
75	1.829	23.45
75	1.829	29.90
75	1.829	28.21
75	4.899	48.85
75	4.899	60.42
75	4.899	42.43
75	4.899	55.28
75	4.899	54.64
75	6.596	47.32
75	6.596	39.24
75	6.596	35.77
75	6.596	40.40
75	6.596	46.74
75	6.596	50.78
90	0.720	14.92
90	0.720	15.31
90	0.720	14.07
90	0.968	13.22
90	0.968	14.65
90	0.968	14.92
90	1.829	13.68
90	1.829	17.59
90	1.829	13.68
90	4.899	28.57
90	4.899	29.71
90	4.899	32.00
90	4.899	29.71
90	4.899	30.28
90	6.596	27.18
90	6.596	29.23
90	6.596	18.98
90	6.596	24.62
90	6.596	22.05

Table S2 Values for mean and standard deviation of number of particles (n_s) adhering per unit area in parallel plate flow chamber experiments

Wall shear rate S [s^{-1}]	Particle diameter d [µm]	Mean adhesion μ[#/mm^2]	Standard deviation σ[#/mm^2]
50	0.72	21.43	4.56
50	0.968	27.45	1.69
50	1.829	39.87	1.24
50	4.899	57.16	6.39
50	6.596	64.00	9.76
75	0.72	19.02	2.15
75	0.968	18.37	1.12
75	1.829	23.29	4.90
75	4.899	52.32	6.88
75	6.596	43.38	5.75
90	0.72	14.77	0.63
90	0.968	14.26	0.91
90	1.829	14.98	2.26
90	4.899	30.05	1.25
90	6.596	24.41	4.06

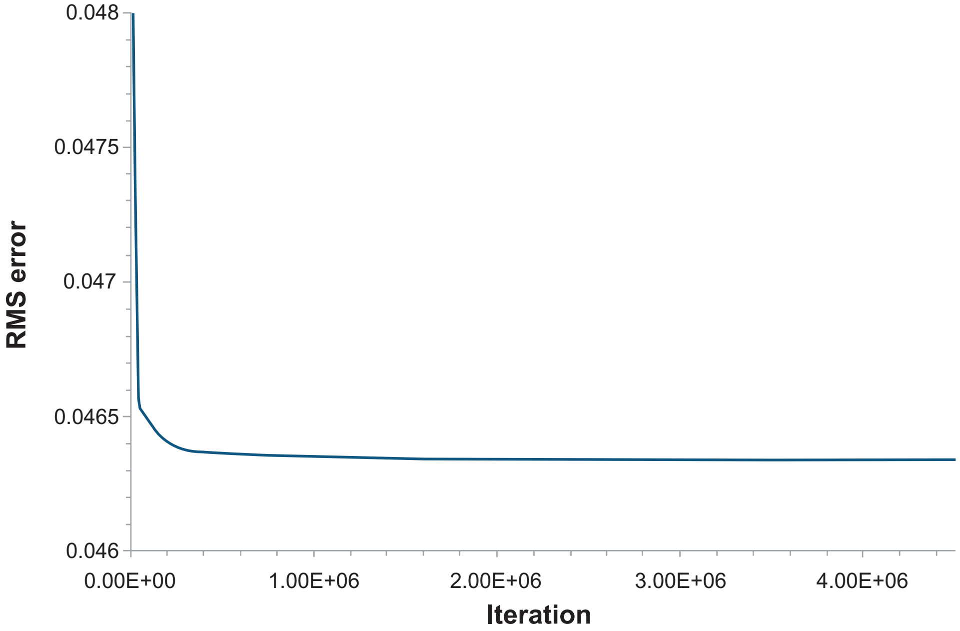

Figure S1 Root mean squared error of the learning set of data for ANN231.

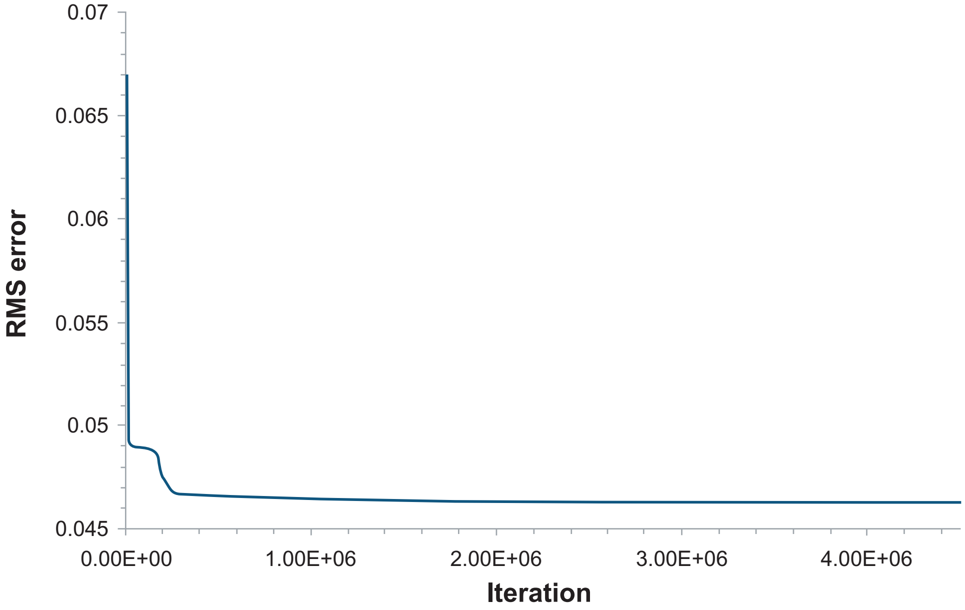

Figure S2 Root mean squared error of the learning set of data for ANN2321.